J. Fluid Mech. (2011), *vol.* 670, *pp.* 176–203. © Cambridge University Press 2011
doi:10.1017/S0022112010005215

Direct numerical simulation of turbulence in injection-driven three-dimensional cylindrical flows

JU ZHANG† AND THOMAS L. JACKSON

Computational Science and Engineering, University of Illinois at Urbana-Champaign, Urbana, IL 61801, USA

(Received 21 January 2010; revised 1 October 2010; accepted 1 October 2010; first published online 19 January 2011)

Incompressible turbulent flow in a periodic circular pipe with strong injection is studied as a simplified model for the core flow in a solid-propellant rocket motor and other injection-driven internal flows. The model is based on a multi-scale asymptotic approach. The intended application of the current study is erosive burning of solid propellants. Relevant analysis for easily accessible parameters for this application, such as the magnitudes, main frequencies and wavelengths associated with the near-wall shear, and the assessment of near-wall turbulence viscosity is focused on. It is found that, unlike flows with weak or no injection, the near-wall shear is dominated by the root mean square of the streamwise velocity which is a function of the Reynolds number, while the mean streamwise velocity is only weakly dependent on the Reynolds number. As a result, a new wall-friction velocity $u_\tau = \sqrt{\tau_w/\rho}$, based on the shear stress derived from the sum of the mean and the root mean square, i.e. $\tau_{w,inj} = \mu|\partial(\bar{u} + u_{rms})/\partial r|_w$, is proposed for the scaling of turbulent viscosity for turbulent flows with strong injection. We also show that the mean streamwise velocity profile has an inflection point near the injecting surface.

Key words: turbulence simulation, turbulent flows

1. Introduction

Erosive burning, a modification of the local burn rate of a solid propellant from its strand burn rate value, has been observed in a variety of solid rocket motors (SRMs) since the 1950s. Erosive burning usually occurs when large crossflow velocities are present, such as in the aft end of a long slender motor, in constricted flow designs (e.g. star-aft grains and slot regions found in star-shaped grains) or in narrow channels adjacent to field joints. The change in the burn rate may be either greater (positive erosion) or less (negative erosion) than the nominal burn rate value obtained in the absence of a crossflow. If the ballistician does not properly take into account erosive burning in the design stage, catastrophic consequences can result. See King (1993) for a review of studies on erosive burning.

The mechanism that leads to the change in the local burn rate of a solid propellant is poorly understood and has been the subject of intense modelling efforts ever since it was first reported in Green (1954). Currently, the predominant theory is

† Email address for correspondence: juzhang@illinois.edu

https://doi.org/10.1017/S0022112010005215 Published online by Cambridge University Press

that turbulent eddies are pushed (convected) closer to the propellant surface as the magnitude of the crossflow velocity increases, thereby increasing the local transport properties (species and thermal diffusion). Since the heat flux at the surface is the mechanism by which a solid propellant burns (e.g. a local energy balance across the solid–gas interface involves the heat flux), increasing the heat flux increases the local burning rate. With an increase in heat flux, the propellant evaporates more quickly, adding more fuel and oxidizer to the flame zone. On the basis of the turbulent eddy theory, a number of erosive-burning models have been constructed. These models assume the turbulent (eddy) viscosity to be of a certain form, and the assumed forms can be different in different works. The theories are based on a turbulent boundary layer either along a flat plate or in a channel with non-transpired walls. This is understandable, as the theories for these types of flows are far more developed than that for turbulent internal flows with transpired walls, which is a more appropriate configuration for an erosive-burning study. Unfortunately, none of the models fit all the data.

It is not immediately clear how turbulence, in the form of small-scale eddies, can survive in a region close to the propellant surface. The local Péclet number, defined as the ratio of convective to diffusive transport, must be of order one for the flame to reside near the propellant surface; if the Péclet number is too large, the flame will be blown off the surface, and the propellant will quench. Since the Péclet number is proportional to the Reynolds number, the local Reynolds number itself must also be of order one. Furthermore, the injection velocity is strong enough to blow off the boundary layer. Thus, the question of turbulence surviving close to the propellant surface becomes important to address.

In contrast to the turbulent eddy theory, we have proposed that turbulence (or acoustics) generates a time-dependent shear flow near the propellant surface which can alter the burning characteristics of the reactants there (Buckmaster & Jackson 2000; Isfahani, Zhang & Jackson 2009; Zhang & Jackson 2010). In these works we assumed that the velocity field near the propellant surface can be described, in two dimensions, by

$$\left.\begin{aligned} u &= A\,\cos\left(\frac{2\pi x}{\lambda}\right)\,\sin(\omega t)\,y, \\ v &= v_{inj} + \frac{A\pi}{\lambda}\sin\left(\frac{2\pi x}{\lambda}\right)\,\sin(\omega t)\,y^2. \end{aligned}\right\} \tag{1.1}$$

Here, $\omega = 2\pi f$ with f (Hz) the frequency, λ (cm) the wavelength, A (s^{-1}) the dimensional shear rate amplitude, v_{inj} ($cm\,s^{-1}$) the dimensional injection velocity, x (cm) the tangential coordinate to the propellant surface and y (cm) the nominal normal coordinate to the propellant surface. For homogeneous propellants we showed that the effect of the shear flow can result in flame stretch, leading to both negative and positive erosion. For heterogeneous propellants, we showed that the flame strengthens (increase in kinetic rate) when a time-dependent shear blows oxidizer gases over fuel regions, but it occurs over a narrower section along the propellant surface, and therefore the integrated heat flux back to the propellant is not significantly larger. On the other hand, when fuel gases are blown over oxidizer particles the reaction rate remains essentially unchanged, but the section of the propellant surface over which reaction occurs increases, and therefore the integrated heat flux also increases, leading to an enhancement of the burning rate. This effect becomes more pronounced when

https://doi.org/10.1017/S0022112010005215 Published online by Cambridge University Press

the oxidizer-particle diameter is larger, a morphology effect that is consistent with experimental observations (King 1993).

The particular form of the shear flow given by (1.1) near the propellant surface is supported by direct numerical simulations (DNS) of wall-injection flows in planar geometries based on a multi-scale approach and can be used to provide estimates for the parameters A, λ and ω. However, SRMs typically have centre-perforated grains and are therefore cylindrical. Thus, the main goals of this paper are to extend the multi-scale model presented in Zhang & Jackson (2010) to cylindrical geometry and to describe the flow characteristics near the injection surface.

DNS for channel or pipe flows with non-transpired walls have been performed in the past by many, e.g. Kim, Moin & Moser (1987), Moser, Kim & Mansour (1999) and Eggels *et al.* (1993). Cabrit & Nicoud (2009) recently performed DNS for reactive flows. For flows with transpired walls, several papers are relevant to our discussion here. Nicoud, Poinsot & Ha Minh (1995) used DNS to examine the turbulent flow between an injecting wall at $y=0$ and a free stream at a distance $y=h$ above the wall. Periodic conditions are imposed in the streamwise (x) and transverse (z) directions. They showed that the high-shear region typically found in non-transpired boundary layers is lifted away from the wall, and as a consequence an inflection point appears in the mean streamwise velocity profile. Sumitani & Kasagi (1995) used DNS to examine a fully turbulent channel flow between an injecting and a suction wall. Similar to the configuration of Nicoud *et al.* (1995), periodic conditions were applied in the streamwise and transverse directions in the work of Sumitani & Kasagi (1995). They showed that the turbulent statistics, as well as most of the classical budgets, are modified near the injecting wall. Because the injection rate is small, the mean streamwise velocity profile does not have an inflection point, and in fact the profile differs little from the non-transpired case near the wall. A linear stability analysis for this configuration was carried out by Nicoud & Angilella (1997). We comment here that the configurations examined above are not appropriate for typical cylindrical rocket motors with circumferential injection; however, for motors with a very large radius it is possible that cylindrical effects might play a minor role in the near-wall region, and a planar geometry would then be relevant.

DNS for a full-scale SRM is still prohibitively expensive in terms of CPU costs and wall-clock time. An alternative is to use a multi-scale analysis and is based on the assumption that both the mean flow and root mean square (r.m.s.) velocities evolve slowly in the axial direction, with the turbulent fluctuations evolving on the fast scale. It has been formulated and used by Spalart (1988) for turbulent boundary layers. Venugopal, Moser & Najjar (2008, and the references therein) extended it to three-dimensional injection-driven plane channel flows, a configuration appropriate for planar SRM computations. Within the SRM context, it determines the flow dynamics at any plane with streamwise location $x/h=1/\epsilon$, where ϵ is a small parameter, x the distance from the head end and h the half-width (radius) of the chamber for a planar (cylindrical) geometry. Asymptotic analysis valid in the limit of vanishing ϵ removes the overall axial gradients and generates a problem with periodic boundary conditions at the upstream and downstream ends in which the gradient effects appear as source terms in the evolution equations. Furthermore, ϵ is a geometric parameter, but it is also the ratio of mass injection rate to the mean flow rate at the location x/h. The validation of the multi-scale analysis for planar geometry was also carried out by comparing the models of the slow-derivative terms in the multi-scale analysis with the statistics gathered from large-eddy simulations (LES) of a spatially evolving flow

https://doi.org/10.1017/S0022112010005215 Published online by Cambridge University Press

in a planar SRM. The authors have shown that the r.m.s. quantities compare well, especially at large streamwise distances from the head end. Overall, the models for the slow-derivative terms were shown to be consistent with the LES of Wasistho & Moser (2005). As mentioned earlier, we extend the multi-scale framework to three-dimensional cylindrical geometry, a geometry more appropriate for centre-perforated SRMs.

With this DNS tool in place, we show that the turbulent (eddy) viscosity is too small near the injection surface to play a role in erosive burning, except perhaps in very large motors. On the other hand, we show that intense time- and space-dependent shear flows exist near the injection surface and are found to be an important ingredient for erosive burning to take place in SRMs.

This paper is organized as follows: § 2 presents the mathematical framework for the multi-scale analysis and derives the appropriate equations for numerical simulations. The numerical method is discussed in § 3. Section 4 presents the numerical results of the multi-scale framework, and a number of important topics are discussed. Finally, conclusions are given in § 5.

2. Mathematical formulation

The model problem that we are considering is appropriate for a centre-perforated grain of an SRM. We consider transpired walls in the circumferential direction (θ) and at a fixed radius (h), with periodic boundary conditions applied in the axial direction (x).

2.1. *Governing equations*

The non-dimensional conservation equations for an incompressible flow to be solved in three-dimensional cylindrical coordinates are

$$\left.\begin{aligned}
&\frac{\partial u_x}{\partial x}+\frac{1}{r}\frac{\partial r u_r}{\partial r}+\frac{1}{r}\frac{\partial u_\theta}{\partial \theta}=0,\\
&\frac{\partial u_x}{\partial t}+(\boldsymbol{V}\cdot\nabla)u_x=-\frac{\partial p}{\partial x}+\frac{1}{Re}\nabla^2 u_x,\\
&\frac{\partial u_r}{\partial t}+(\boldsymbol{V}\cdot\nabla)u_r-\frac{1}{r}u_\theta^2=-\frac{\partial p}{\partial r}+\frac{1}{Re}\left(\nabla^2 u_r-\frac{u_r}{r^2}-\frac{2}{r^2}\frac{\partial u_\theta}{\partial \theta}\right),\\
&\frac{\partial u_\theta}{\partial t}+(\boldsymbol{V}\cdot\nabla)u_\theta+\frac{u_r u_\theta}{r}=-\frac{1}{r}\frac{\partial p}{\partial \theta}+\frac{1}{Re}\left(\nabla^2 u_\theta+\frac{2}{r^2}\frac{\partial u_r}{\partial \theta}-\frac{u_\theta}{r^2}\right),
\end{aligned}\right\} \tag{2.1}$$

where

$$\left.\begin{aligned}
\boldsymbol{V}\cdot\nabla&=u_x\frac{\partial}{\partial x}+u_r\frac{\partial}{\partial r}+\frac{1}{r}u_\theta\frac{\partial}{\partial \theta},\\
\nabla^2&=\frac{\partial^2}{\partial x^2}+\frac{1}{r}\frac{\partial}{\partial r}\left(r\frac{\partial}{\partial r}\right)+\frac{1}{r^2}\frac{\partial^2}{\partial \theta^2}.
\end{aligned}\right\} \tag{2.2}$$

Here, lengths are scaled by h, the cylinder radius; velocities by v_{inj}, the velocity at the injection surface; and time by h/v_{inj}. Note that we reserve these particular symbols, i.e. h, v_{inj} and also ν (kinematic viscosity) and L (chamber length), for dimensional scales throughout the paper. Also, (u_x, u_r, u_θ) are the velocity components in the (x, r, θ)

https://doi.org/10.1017/S0022112010005215 Published online by Cambridge University Press

directions, respectively; p is the pressure; and $Re_{inj} = v_{inj}h/\nu$ is the injection Reynolds number. We also perform simulations of flows with non-transpired walls. In this case, the velocities are scaled by the wall-friction velocity $u_\tau = \sqrt{\tau_w/\rho}$, and the Reynolds number is then given by $Re_\tau = u_\tau h/\nu$.

We also consider the planar configuration for the purpose of verification of the numerical solver. Thus, the non-dimensional conservation equations in planar geometry are given by

$$\left.\begin{aligned} &\frac{\partial u}{\partial x} + \frac{\partial v}{\partial y} + \frac{\partial w}{\partial z} = 0, \\ &\frac{\partial u}{\partial t} + (\boldsymbol{V}\cdot\nabla)u = -\frac{\partial p}{\partial x} + \frac{1}{Re}\nabla^2 u, \\ &\frac{\partial v}{\partial t} + (\boldsymbol{V}\cdot\nabla)v = -\frac{\partial p}{\partial y} + \frac{1}{Re}\nabla^2 v, \\ &\frac{\partial w}{\partial t} + (\boldsymbol{V}\cdot\nabla)w = -\frac{\partial p}{\partial z} + \frac{1}{Re}\nabla^2 w, \end{aligned}\right\} \tag{2.3}$$

where

$$\left.\begin{aligned} &\boldsymbol{V}\cdot\nabla = u\frac{\partial}{\partial x} + v\frac{\partial}{\partial y} + w\frac{\partial}{\partial z}, \\ &\nabla^2 = \frac{\partial^2}{\partial x^2} + \frac{\partial^2}{\partial y^2} + \frac{\partial^2}{\partial z^2}. \end{aligned}\right\} \tag{2.4}$$

The equations are non-dimensionalized by the same scalings as in the cylindrical case, except here h is the channel half-height rather than the radius.

2.2. *Multi-scale analysis*

In the spirit of multi-scale analysis (Spalart 1988), we introduce the following 'slow' and 'fast' variables in the streamwise direction:

$$x_s = \epsilon x, \quad x_f = x, \tag{2.5}$$

where ϵ is a small parameter. In the context of an SRM, it determines the streamwise location $X/h = 1/\epsilon$, where X is the distance from the head end and h is the half-width (radius) of the chamber for a planar (cylindrical) geometry; ϵ is also the ratio of the mass injection rate to the mean flow rate at the location X (Venugopal *et al.* 2008).

For $\epsilon \ll 1$, x_f changes much more rapidly than x_s. The spatial derivatives become

$$\left.\begin{aligned} &\frac{\partial}{\partial x} \to \frac{\partial}{\partial x_f} + \epsilon\frac{\partial}{\partial x_s}, \\ &\frac{\partial^2}{\partial x^2} \to \frac{\partial^2}{\partial x_f^2} + 2\epsilon\frac{\partial^2}{\partial x_f \partial x_s} + \epsilon^2\frac{\partial^2}{\partial x_s^2}. \end{aligned}\right\} \tag{2.6}$$

Neglecting the slow-derivative terms $O(\epsilon/Re)$ or higher that appear in the viscous terms, the conservation equations (2.1) can then be transformed into the following

https://doi.org/10.1017/S0022112010005215 Published online by Cambridge University Press

multi-scale formulation:

$$\left.\begin{aligned}
&\frac{\partial u_x}{\partial x_f}+\epsilon\frac{\partial u_x}{\partial x_s}+\frac{1}{r}\frac{\partial r u_r}{\partial r}+\frac{1}{r}\frac{\partial u_\theta}{\partial \theta}=0,\\
&\frac{\partial u_x}{\partial t}+u_x\frac{\partial u_x}{\partial x_f}+\epsilon u_x\frac{\partial u_x}{\partial x_s}+u_r\frac{\partial u_x}{\partial r}+\frac{1}{r}u_\theta\frac{\partial u_x}{\partial \theta}=-\frac{\partial p}{\partial x_f}-\epsilon\frac{\partial p}{\partial x_s}+\frac{1}{Re}\nabla^2 u_x,\\
&\frac{\partial u_r}{\partial t}+u_x\frac{\partial u_r}{\partial x_f}+\epsilon u_x\frac{\partial u_r}{\partial x_s}+u_r\frac{\partial u_r}{\partial r}+\frac{1}{r}u_\theta\frac{\partial u_r}{\partial \theta}-\frac{1}{r}u_\theta^2\\
&\qquad\qquad=-\frac{\partial p}{\partial r}+\frac{1}{Re}\left(\nabla^2 u_r-\frac{u_r}{r^2}-\frac{2}{r^2}\frac{\partial u_\theta}{\partial \theta}\right),\\
&\frac{\partial u_\theta}{\partial t}+u_x\frac{\partial u_\theta}{\partial x_f}+\epsilon u_x\frac{\partial u_\theta}{\partial x_s}+u_r\frac{\partial u_\theta}{\partial r}+\frac{1}{r}u_\theta\frac{\partial u_\theta}{\partial \theta}+\frac{u_r u_\theta}{r}\\
&\qquad\qquad=-\frac{1}{r}\frac{\partial p}{\partial \theta}+\frac{1}{Re}\left(\nabla^2 u_\theta+\frac{2}{r^2}\frac{\partial u_r}{\partial \theta}-\frac{u_\theta}{r^2}\right).
\end{aligned}\right\}\tag{2.7}$$

2.3. *Modelling the slow derivatives*

The remaining task in solving (2.7) is the modelling of the 'slow-derivative' terms $\partial/\partial x_s$. To have an approximation of $\partial u/\partial x_s$ in the context of turbulent flows, we assume that the mean streamwise velocity U does not depend on x_f and takes the form

$$U=U(x_s,r,\theta)=\frac{1}{\epsilon}U_0(r,\theta)x_s+U_1(x_s,r,\theta)+\epsilon U_2(x_s,r,\theta)+\cdots\approx\frac{1}{\epsilon}U_0(r,\theta)x_s.\tag{2.8}$$

Note that we temporarily drop the subscript x. The fact that the leading term in the above expansion has a linear dependence on x_s is inspired by the Taylor–Proudman–Culick solution (Taylor 1956; Proudman 1960; Culick 1966; hereafter, we will refer to it as Culick's solution for brevity and the focus on cylindrical geometry). We also drop the terms of order higher than $1/\epsilon$ for a reasonably good approximation of U.

Next, taking the derivative with respect to x_s of the above equation, we obtain

$$\frac{\partial U}{\partial x_s}\approx\frac{1}{\epsilon}U_0(r,\theta).\tag{2.9}$$

For streamwise location $\tilde{x}=1/\epsilon$ (in the original full-scale rather than the multi-scale configuration),

$$x_s=\epsilon\tilde{x}=1.\tag{2.10}$$

We, therefore, have the following for this streamwise location from (2.8):

$$U=U(x_s=1,r,\theta)\approx\frac{1}{\epsilon}U_0(r,\theta).\tag{2.11}$$

On the basis of this equation and (2.9), we have

$$\frac{\partial U}{\partial x_s}\approx\frac{1}{\epsilon}U_0(r,\theta)\approx U.\tag{2.12}$$

Similarly, we assume that u-r.m.s. (or any other r.m.s. quantity) also has a linear dependence on x_s, i.e.

$$u_{rms}\approx\frac{1}{\epsilon}u_{0,rms}x_s,\tag{2.13}$$

https://doi.org/10.1017/S0022112010005215 Published online by Cambridge University Press

which seems to be a reasonably good assumption to the extent that further downstream from the head end the r.m.s. is stronger. Therefore, we have the u-r.m.s. counterpart of (2.12) for the streamwise location $\tilde{x} = 1/\epsilon$ (where $x_s = 1$ and $u_{rms} = (1/\epsilon)u_{0,rms}$), i.e.

$$\frac{\partial u_{rms}}{\partial x_s} \approx \frac{1}{\epsilon} u_{0,rms} \approx u_{rms}, \tag{2.14}$$

which is also the assumption made by Venugopal *et al.* (2008).

For the approximation of $\partial u/\partial x_s$, we now have

$$\frac{\partial u}{\partial x_s} = \frac{\partial (U + u')}{\partial x_s} \approx U + u_{rms} u'_p = u, \tag{2.15}$$

giving rise to the formulations of the source terms of the continuity equation and the x-momentum equation. Here, $u' = u_{rms} u'_p$ and u'_p is a function independent of x_s (Venugopal *et al.* 2008). For the approximation of $\partial u_r/\partial x_s$ or $\partial u_\theta/\partial x_s$, we only need to invoke the $\partial u'_r/\partial x_s$ and $\partial u'_\theta/\partial x_s$ counterparts of the slow derivative of the r.m.s. quantities, as the mean u_r and u_θ are independent of x in the full-scale configuration. Therefore, we have

$$\left.\begin{aligned} \frac{\partial u_r}{\partial x_s} &= \frac{\partial u'_r}{\partial x_s} \approx u'_r, \\ \frac{\partial u_\theta}{\partial x_s} &= \frac{\partial u'_\theta}{\partial x_s} \approx u'_\theta. \end{aligned}\right\} \tag{2.16}$$

Finally, for the slow derivative of mean pressure, we first have

$$\bar{p} = \bar{p}(x_s) = \frac{1}{\epsilon^2}\bar{p}_0 x_s^2 + \frac{1}{\epsilon}\bar{p}_1(x_s) + \bar{p}_2(x_s) + \cdots \approx \frac{1}{\epsilon^2}\bar{p}_0 x_s^2. \tag{2.17}$$

The fact that the leading term in the above expansion has the quadratic dependence on x_s is again inspired by Culick's solution. We next drop the terms of order higher than $1/\epsilon^2$, set $\bar{p}_0 = -\pi^2/2$ according to Culick's solution and take the derivative with respect to x_s of the above equation to obtain

$$\frac{\partial \bar{p}}{\partial x_s} \approx -\frac{\pi^2}{\epsilon^2} x_s. \tag{2.18}$$

Again, recognizing the fact that for the streamwise location $\tilde{x} = 1/\epsilon$, x_s is equal to 1, we have

$$\frac{\partial \bar{p}}{\partial x_s} \approx -\frac{\pi^2}{\epsilon^2}. \tag{2.19}$$

Similarly for planar geometry,

$$\frac{\partial \bar{p}}{\partial x_s} = -\frac{\pi^2}{4\epsilon^2}. \tag{2.20}$$

Furthermore, $\partial \bar{p}/\partial r$ and $\partial \bar{p}/\partial \theta$ are assumed to be zero.

2.4. *Validity of the slow-derivative models*

It was noted in the Introduction that the validation of the slow-derivative models in planar geometry was carried out in Venugopal *et al.* (2008). There, the authors validated the models for the slow-derivative terms by comparison with statistics from an LES of the spatially evolving flow in a planar model of an SRM (Wasistho & Moser 2005). The statistics, in turn, were validated against the cold-flow experiments of Traineau, Hervat & Kuentzmann (1986). The authors showed that the models

https://doi.org/10.1017/S0022112010005215 Published online by Cambridge University Press



FIGURE 1. Vorticity contours for a typical planar (two-dimensional) motor. The length of the chamber is $L = 4.5$ m, and the chamber half-height is $h = 0.1$ m; 10 % white noise is added to the injection rate.

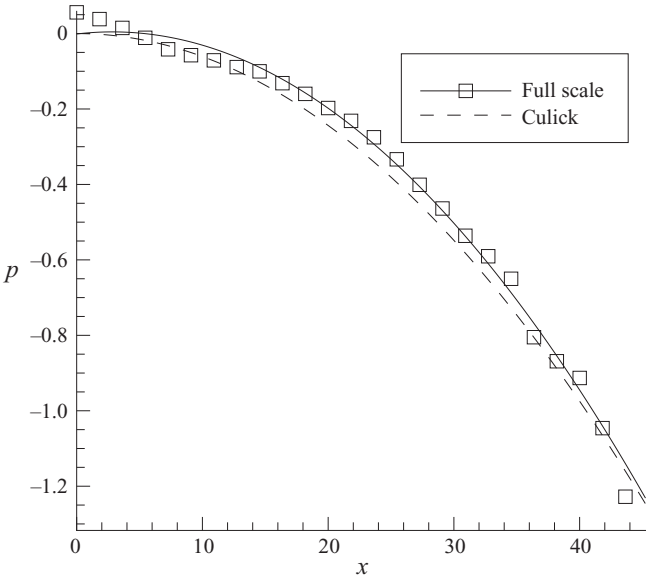


FIGURE 2. Plot of pressure for a one-dimensional slice through the motor shown in figure 1. The dashed curve corresponds to Culick's solution. The pressure is scaled by $\rho v_{inj}^2 L^2/h^2$.

for the slow-derivative terms and the self-similar assumption for $\overline{\rho u}$ break down close to the nozzle region, while the r.m.s. quantities remain good, especially at large streamwise distances from the head end (this corresponds to small values of ϵ). For larger values of ϵ, i.e. near the head end, the models for the slow derivatives of r.m.s. quantities do not agree well with the LES (figure 3c of Venugopal *et al.* 2008), where the transition from laminarity to turbulence occurs.

In our context, for incompressible flows, we expect the self-similarity assumption of $\bar{u}$ to be well approximated by Culick's solution, since it is exact for an inviscid flow; the model for the slow-derivative term therefore naturally follows. The validity of the assumption for $\partial\bar{p}/\partial x_s$ is sought through a simulation of a planar motor configuration (see figure 1). Figure 2 plots the pressure as a function of x for the simulation (solid line). The numerical solution is compared with Culick's solution for pressure (dashed line), given by $p = -(\pi^2 x^2)/(8(L/h)^2)$. The pressures are scaled by $\rho v_{inj}^2 L^2/h^2$, where v_{inj} is the injection velocity, L the chamber length and h the chamber half-width. Note that the agreement is excellent, which validates the modelling of the slow-derivative term for the pressure gradient.

3. Simulation details

3.1. *Numerical method*

Equations (2.7) are solved using the high-order incompressible scheme described and verified by Zhang & Jackson (2009), extended here to cylindrical geometry.

https://doi.org/10.1017/S0022112010005215 Published online by Cambridge University Press

In particular, the convective terms are discretized using the fifth-order weighted essentially non-oscillatory (WENO) scheme of Jiang & Shu (1996). The fractional-step scheme of Kim & Moin (1985), together with the optimized two-step alternating four–six low-dissipation and low-dispersion Runge–Kutta (LDDRK) scheme of Hu, Hussaini & Manthey (1996), is used to improve temporal accuracy. The solver accurately captures the Taylor–Proudman–Culick analytical solution for a steady flow in a slender chamber.

The numerical behaviour at $r=0$ in both axisymmetric and three-dimensional cylindrical geometries needs to be regularized to avoid the removable singularity. For velocity components at $r=0$ an averaging over the first grid points away from $r=0$ over 2π in the $r\theta$-plane is carried out. To this end, u_x is simply averaged from u_x on those grid points. The other velocity components u_r and u_θ are first transformed into Cartesian geometry as u_y and u_z, i.e. for the jth grid point in θ,

$$u_{y,j} = u_{r,j}\sin(\theta) + u_{\theta,j}\cos(\theta), \tag{3.1}$$

$$u_{z,j} = u_{r,j}\cos(\theta) - u_{\theta,j}\sin(\theta), \tag{3.2}$$

and averaged in Cartesian geometry,

$$u_y|_{r=0} = \frac{1}{n_\theta}\sum_{j=1}^{n_\theta}(u_{r,j}\sin(\theta) + u_{\theta,j}\cos(\theta)), \tag{3.3}$$

$$u_z|_{r=0} = \frac{1}{n_\theta}\sum_{j=1}^{n_\theta}(u_{r,j}\cos(\theta) - u_{\theta,j}\sin(\theta)). \tag{3.4}$$

This transform is necessary because these grid points can be seen as close neighbours in both the y-direction and the z-direction but not in the θ-direction. The unique velocity vector obtained in this way is transformed back into cylindrical geometry when necessary.

The numerical scheme of Zhang & Jackson (2009) requires that the pressure update is solved using a Poisson equation. To avoid the removable singularity at $r=0$, instead of solving

$$\nabla^2 p = \left\{\frac{1}{r}\frac{\partial}{\partial r}\left(r\frac{\partial}{\partial r}\right) + \frac{1}{r^2}\frac{\partial^2}{\partial\theta^2} + \frac{\partial^2}{\partial x^2}\right\} p = S, \tag{3.5}$$

we solve

$$r^2\nabla^2 p = \left\{r\frac{\partial}{\partial r}\left(r\frac{\partial}{\partial r}\right) + \frac{\partial^2}{\partial\theta^2} + r^2\frac{\partial^2}{\partial x^2}\right\} p = r^2 S \tag{3.6}$$

in three-dimensional cylindrical geometry or solve

$$r\nabla^2 p = \left\{\frac{\partial}{\partial r}\left(r\frac{\partial}{\partial r}\right) + r\frac{\partial^2}{\partial x^2}\right\} p = rS \tag{3.7}$$

in axisymmetric geometry. In (3.5)–(3.7), S is related to the discrete divergence of the intermediate velocity in the fractional-step method (Kim & Moin 1985).

To resolve the velocity gradient in the wall-normal direction, a stretched grid is used. Define the following transform:

$$r = 1 - a(1-\eta) - b(1-\eta)^2, \tag{3.8}$$

where $a=3-4\alpha$ and $b=4\alpha-2$. Here, α is a parameter that controls the strength of the stretching. The greater the value of α, the stronger the stretch; i.e. the resolution near the wall at $r=1$ will be finer. Also note that the value of α should be chosen so

https://doi.org/10.1017/S0022112010005215 Published online by Cambridge University Press

that no singularity in the transformation of the spatial derivatives is introduced. The computational grid is $0 \leqslant \eta \leqslant 1$, and under this transform we have

$$\frac{\partial}{\partial x} \rightarrow \frac{\partial}{\partial x}, \tag{3.9}$$

$$\frac{\partial}{\partial r} \rightarrow \frac{\mathrm{d}\eta}{\mathrm{d}r}\frac{\partial}{\partial \eta}, \tag{3.10}$$

$$\frac{\partial^2}{\partial r^2} \rightarrow \left(\frac{\mathrm{d}\eta}{\mathrm{d}r}\right)^2 \frac{\partial^2}{\partial \eta^2} + \frac{\mathrm{d}^2\eta}{\mathrm{d}r^2}\frac{\partial}{\partial \eta}, \tag{3.11}$$

where

$$\frac{\mathrm{d}\eta}{\mathrm{d}r} = \frac{1}{a + 2b(1-\eta)}, \qquad \frac{\mathrm{d}^2\eta}{\mathrm{d}r^2} = \frac{2b}{(a + 2b(1-\eta))^3}. \tag{3.12}$$

Similarly for planar geometry, we define the same transform as in (3.8) for $0 \leqslant y \leqslant 1$ with an antisymmetric profile about $y = 0$.

3.2. *Validation for weak injection*

Because of the lack of a well-developed theory for turbulent internal flows with strong injection ($v_{inj}/U_m > \sim 0.01$), our verification/validation study here consists of DNS of turbulent channel and pipe flows with non-transpired walls or with transpired walls with weak injection ($v_{inj}/U_m \sim 0.001$), both of which do have well-developed theories to compare the results with. Here, U_m is the bulk mean velocity, and the superscript $+$ denotes quantities scaled by wall variables, e.g. $y^+ = yu_\tau/\nu$, $u^+ = \bar{u}/u_\tau$ and $v_{inj}^+ = v_{inj}/u_\tau$, where u_τ is the wall-friction velocity given by (3.15). We comment that there are fundamental differences between turbulent flows with weak wall injection, where a boundary layer along the wall still exists, and turbulent flows with strong wall injection, where the boundary layer is 'blown off'. However, the verification/validation study of the weak injection case can still serve as a partial validation for the numerical solver for strong injection flows, the actual focus of the current work.

Hereafter, unless otherwise noted, channel or pipe refers to flows with non-transpired walls or transpired walls with weak injection, while planar and cylindrical multi-scale simulations refer to flows with strong injection. The governing equations to be solved for pipe flows are given by (2.1) instead of (2.7) (equivalently for channel flow).

The size of the computational domain is $L_x \times L_y \times L_z = [0, 4\pi] \times [-1, 1] \times [0, 2\pi]$ for channel flows and $L_x \times L_r \times L_\theta = [0, 4\pi] \times [0, 1] \times [0, 2\pi]$ for pipe flows. A total of three simulations are performed in this section: case A corresponds to a channel flow without transpiration; case B corresponds to a pipe flow without transpiration; and case C corresponds to a pipe flow with transpiration with $v_{inj}^+ = 0.022$. The Reynolds number based on wall-friction velocity (see the discussion below), Re_τ, is 140 for case A, 141 for case B and 128 for case C. The number of grid points is 128^3 for all cases. The corresponding near-wall resolutions are $\Delta y^+ = 0.15$ with an α of 0.736 for case A and $\Delta r^+ = 0.14$ and 0.13 with an α of 0.72 for cases B and C, respectively.

Results are shown in figure 3 for case A and figure 4 for cases B (solid lines) and C (dot-dashed lines). The dashed curves in each figure correspond to the appropriate theories for turbulent flow. In figure 4(a), the mean velocity u^+ is plotted, while in figure 4(b) an effective mean u_{eff}^+ is plotted. The modified mean velocity is based on

https://doi.org/10.1017/S0022112010005215 Published online by Cambridge University Press

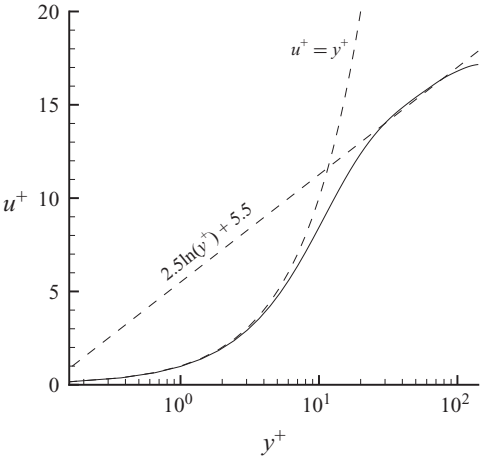


FIGURE 3. Plot of u^+ as a function of distance from the surface for turbulent channel flow (case A). Also shown as the dashed curves are profiles for the theory. Note that $y^+ = yu_\tau/\nu$.

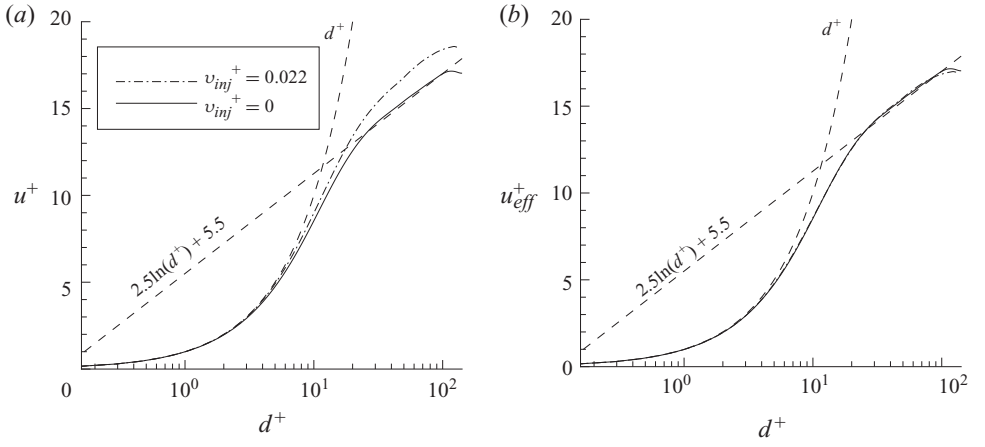


FIGURE 4. Plot of (*a*) u^+ and (*b*) u^+_{eff} as a function of distance from the surface for turbulent pipe flow. Here, case B is denoted by the solid lines, case C by the dot-dashed lines and the theory by the dashed lines; u^+_{eff} is given by (3.13). Note that $d^+ = ((1-r)u_\tau)/\nu$.

Stevenson (1963), given by

$$u^+_{eff} = \frac{2}{v^+_{inj}}\left[\left(1 + v^+_{inj}u^+\right)^{1/2} - 1\right], \tag{3.13}$$

and shows that there exists a scaling between no injection and weak injection. In all cases, good agreement is obtained between the simulations and the theory. Since the theory compares well with experimental data, the study here serves as both verification and validation in the limit of weak injection.

We also examine the near-wall turbulent (eddy) viscosity, defined by

$$-\overline{u'v'} = \nu_t \frac{\partial \overline{u}}{\partial y} \quad \text{(planar)}, \qquad -\overline{u'_x u'_r} = \nu_t \left| \frac{\partial \overline{u}_x}{\partial r} \right| \quad \text{(cylindrical)}. \tag{3.14}$$

https://doi.org/10.1017/S0022112010005215 Published online by Cambridge University Press

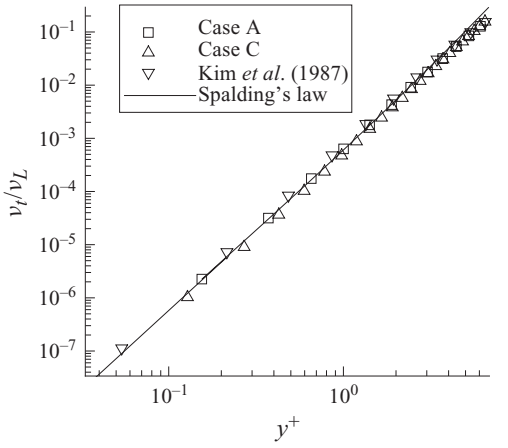


FIGURE 5. Plot of ν_t/ν_L as a function of y^+; for pipe flow, $y^+ = d^+$. The symbols are as follows: □, case A; △, case C; ▽, Kim *et al.* (1987). Spalding's law (Spalding 1961) is denoted by the solid line.

For turbulent channel/pipe flows, the velocity is classically scaled by the wall-friction velocity

$$u_\tau = \sqrt{\tau_w/\rho}, \tag{3.15}$$

where

$$\tau_w = \mu \left.\frac{\partial \bar{u}}{\partial y}\right|_w \quad \text{(planar)}, \qquad \tau_w = \mu \left|\frac{\partial \bar{u}_x}{\partial r}\right|_w \quad \text{(cylindrical)}. \tag{3.16}$$

Values of ν_t/ν_L are plotted in figure 5, where ν_L is the laminar viscosity. The figure shows excellent agreement of our DNS results with the theory and the DNS results of Kim *et al.* (1987). The results of Kim *et al.* (1987) are taken from their table 2, where $-\overline{u'^+v'^+} = -\overline{u'v'}/u_\tau^2 = \nu_t/\nu_L$. DeGraff & Eaton (2000) obtained a power fit of $0.0009(y^+)^3$ from their experimental data, which is a reasonable fit to the current data.

4. Simulation results

In this section results for strong injection are presented. These results make use of the multi-scale equations (2.7).

4.1. *Grid resolution*

We first present a grid resolution study in terms of resolving the r.m.s. velocities. Unless otherwise noted, the size of the computational domain is $L_x \times L_r \times L_\theta = [0, 2\pi] \times [0, 1] \times [0, 2\pi]$. The Reynolds number is taken to be the injection Reynolds number ($Re_{inj} = v_{inj}h/\nu$). As we shall discuss later, unlike channel/pipe flows with non-transpired walls, the r.m.s. of u_x is greater than the mean in a small region at the wall. Thus, it is critical to resolve the r.m.s. velocities in the near-wall region. To show grid convergence, two uniform grids of 64^3 and 128^3 and two stretched grids with $\alpha = 0.689$ and 0.72 in (3.8) are considered. The total number of grid points in the two stretched grids is held fixed with 128^3 points, with a uniform grid in both the x-direction and the θ-direction and a stretched grid in the r-direction. We denote the stretched grids by n^*, where $1/n$ is the near-wall resolution. Thus, the near-wall

https://doi.org/10.1017/S0022112010005215 Published online by Cambridge University Press

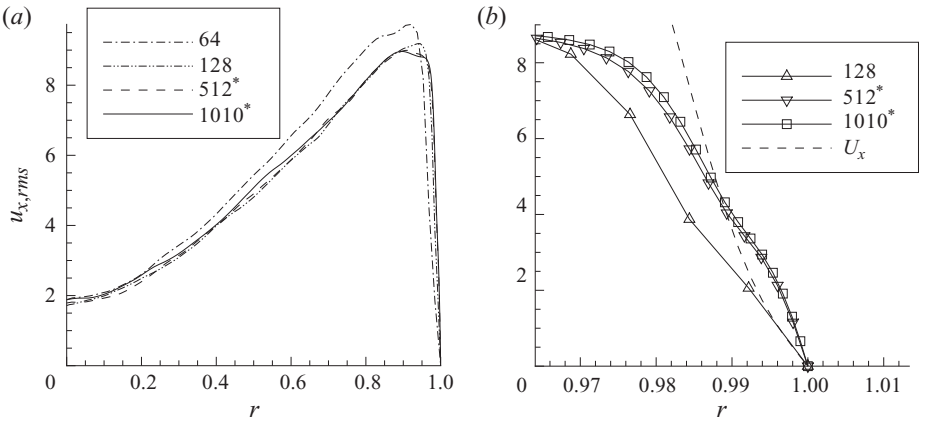


FIGURE 6. (*a*) Plot of the u_x-r.m.s. velocity for the three-dimensional cylindrical multi-scale simulation with $Re_{inj} = 1000$ and $\epsilon = 0.04$ and for uniform and stretched grids. Stretched grids are denoted by n^*, where $1/n$ is the near-wall resolution. (*b*) Close-up view of (*a*) near the wall.

resolutions for the 512* and 1010* grids are 1/512 and 1/1010 with α values of 0.689 and 0.72, respectively.

Figure 6 shows the u_x-r.m.s. velocity for $Re_{inj} = 1000$ and $\epsilon = 0.04$ for the different grid resolutions. Convergence is achieved for the profiles away from the wall at $r < 0.97$, even for the uniform grids. However, in the near-wall region, convergence is only achieved for the two stretched grids, as seen in figure 6(*b*), showing the enlarged view of the near-wall region. Also shown in figure 6(*b*) is the mean of the u_x velocity component U_x, the magnitude of which is smaller than the r.m.s. near the wall. This implies that the flow can oscillate upstream and downstream, a fact also observed for planar geometry (Isfahani *et al.* 2009). However, the thickness of the oscillating layer, defined as the location at which the mean and the r.m.s. are equal, is approximately 0.01 and is significantly thinner compared with $\sim$0.05 and $\sim$0.03 in the two- and three-dimensional planar geometries, respectively. It is worthwhile noting that the resolution requirement in resolving the mean profile is less stringent than that for the r.m.s. because of the smaller near-wall gradient of the mean profile compared with that of the r.m.s. In fact, the U_x profile differs little between the solutions from the 128^3 uniform grid and those from the stretched grids. Convergence is also observed for the other r.m.s. velocity components (not shown here).

As we observed in the above grid resolution study, the criterion for convergence can be quite specific, depending on the particular metric one is interested in. For example, we have shown that in the regions with moderate gradients (i.e. away from the wall), no stringent requirement on the grid resolution seems necessary; even a grid without resolving the near-wall region seems adequate. However, sufficiently high resolution is necessary in the near-wall region if one is focusing on that region. This is the case here as we estimate the shear parameters at the wall. Similarly, the resolution may be adequate for the mean profile, yet it may be inadequate for the r.m.s. (In the case of non-transpired walls, it may be vice versa.) Therefore, we shall be as specific as possible when discussing grid convergence issues throughout the paper, and the next numerical test demonstrates another example of it.

The following test is intended for assessing the adequacy of the grid resolution in the streamwise x-direction. Two simulations are performed, one corresponding to the 512* case ($n_x = 128$) and one with twice as many grid points in the streamwise

https://doi.org/10.1017/S0022112010005215 Published online by Cambridge University Press

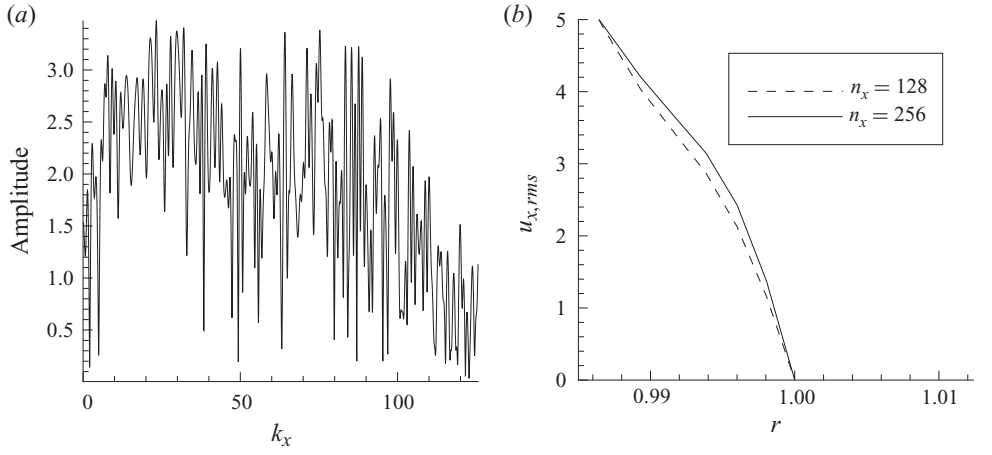


FIGURE 7. (*a*) Plot of the FFT of a one-dimensional slice of u_x in the x-direction along the first grid point away from the wall with $n_x = 256$. (*b*) Plot of near-wall profiles of the r.m.s. velocity of u_x for $n_x = 128$ (dashed line) and 256 (solid line). Here, $Re_{inj} = 1000$, $\epsilon = 0.04$ and 512* is used in the r-direction.

direction ($n_x = 256$). The adequacy of the grid resolution in the streamwise direction can be assessed by examining the energy spectrum, as was done in Venugopal *et al.* (2008), or here with the fast Fourier transforms (FFTs) of one-dimensional slices through the flow field. Figure 7(*a*) plots the FFT of a one-dimensional slice of u_x in the x-direction along the first grid point away from the wall. The grid resolution of $n_x = 256$ is marginally adequate, since there are still appreciable strengths at high wavenumbers. On the other hand, the profile in the wall-normal direction is relatively insensitive to the grid resolution in the x-direction, as can be seen in figure 7(*b*). The wall-normal gradients of u_x-r.m.s., $\partial u_{x,rms}/\partial r$, at the wall are -560 and -665 for $n_x = 128$ and 256, respectively. These are reasonably close with a relative difference of approximately 16 % and are adequate for estimating the shear parameters near the wall for erosive-burning modelling. If the convergence at some distance away from the wall (discussed above for figure 6) can be termed as 'regional independence' (somewhat analogous to using the Euler solution to approximate viscous flow away from the wall), the insensitivity of the profiles in the wall-normal direction to the grid resolution in the x-direction may be referred to as 'directional independence'. We have taken advantage of these independences, especially the directional independence, for the estimate of the shear rate, and have fixed the grid resolution with $n_x = 128$ as a default resolution for the current work.

We do, however, demonstrate that when applying the solver to the Reynolds number regime that should be resolved by DNS, the solutions converge for all the metrics. This is the case for moderate Reynolds numbers. Figure 8 plots the FFT of a one-dimensional slice of u_x along the first grid point away from the wall. Here, the Reynolds number is 200 and ϵ is 0.04. The number of grid points is 256 in x. The power at high wavenumbers, k_x, decreases significantly, indicating sufficient resolution. Among other metrics, the convergence of the profile of the r.m.s. velocity in the wall normal direction is also achieved (not shown here).

4.2. *Turbulent flow fields*

Previous studies (Venugopal *et al.* 2008; Isfahani *et al.* 2009) of the planar configuration have quantified the effects of the streamwise location on the flow

https://doi.org/10.1017/S0022112010005215 Published online by Cambridge University Press

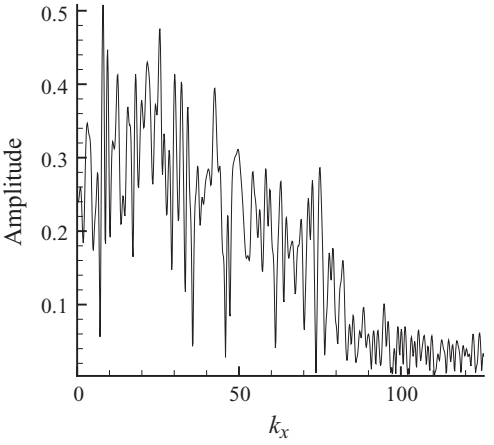


FIGURE 8. Plot of the FFT of a one-dimensional slice in the x-direction of u_x along the first grid point away from the wall for $Re_{inj} = 200$ and $\epsilon = 0.04$; 512* is used in the r-direction.

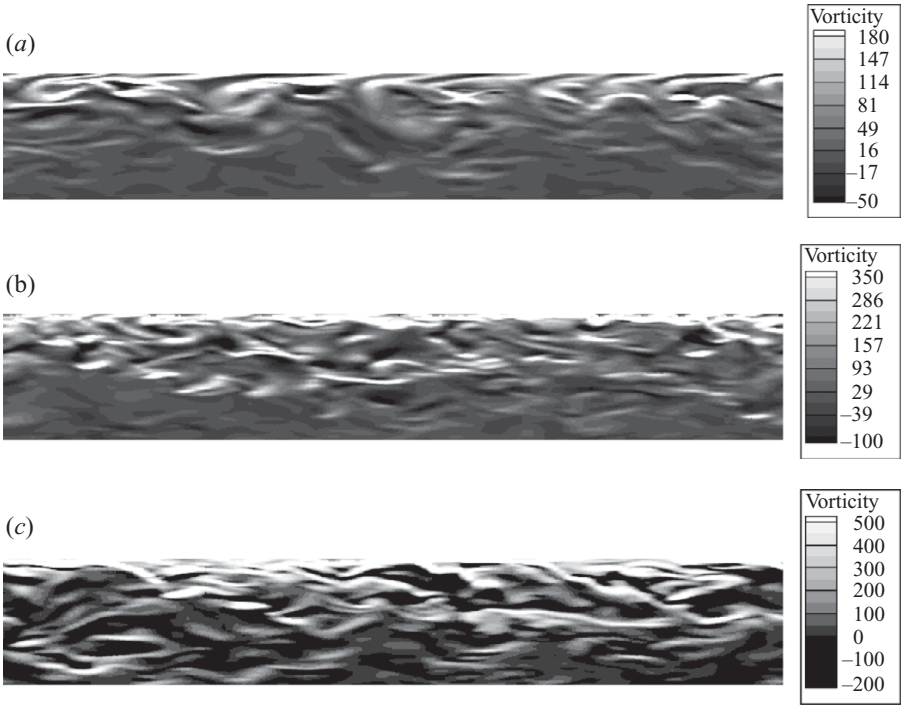


FIGURE 9. Contours of the instantaneous circumferential vorticity ω_θ fields for three-dimensional cylindrical multi-scale simulations with $Re_{inj} = 1000$ and $\epsilon = (a)$ 0.1, (b) 0.04 and (c) 0.025.

dynamics. Near the head end the flow is less turbulent than towards the aft end. Not surprisingly, this is also true for the three-dimensional cylindrical configuration as can be appreciated by examining figure 9, where the instantaneous circumferential vorticity ω_θ fields are plotted for ϵ values of 0.1, 0.04 and 0.025. As in the planar configuration, the vortices are stronger further downstream ($\epsilon = 0.025$) than near the head end ($\epsilon = 0.1$). Close inspection of the vorticity field for $\epsilon = 0.1$ reveals parietal

https://doi.org/10.1017/S0022112010005215 Published online by Cambridge University Press

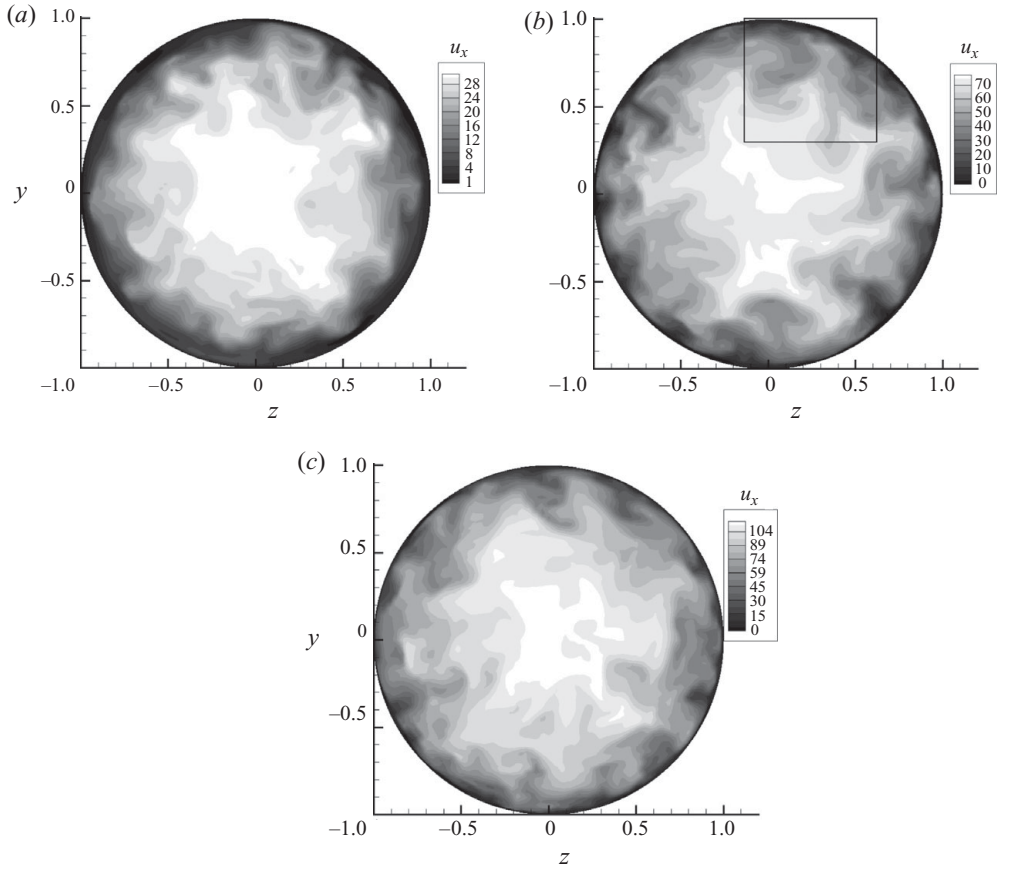


FIGURE 10. Instantaneous streamwise velocity fields in the $r\theta$-plane for ϵ values of (a) 0.1, (b) 0.04 and (c) 0.025, corresponding to those shown in figure 9.

vortex shedding that is more clearly observed for two-dimensional configurations (Lupoglazoff & Vuillot 1996, 1998; Avalon *et al.* 2000; Apte & Yang 2003).

Instantaneous streamwise velocity fields in the $r\theta$-plane are plotted in figure 10 for the values of ϵ corresponding to those shown in figure 9. The flow structures seem to be dominated by large-scale coherent structures for all values of ϵ. An enlarged view of a coherent structure marked by the black box in figure 10(b) for $\epsilon = 0.04$ is shown in figure 11, along with the (u_r, u_θ) velocity vectors. The coherent structure can be appreciated by the vortex centred around $(z, y) = (0.15, 0.5)$. The length scale of $\Delta\theta \sim \pi/4$ of the coherent structure is captured well by an FFT of the one-dimensional slice through $r = 0.5$, shown in figure 12. Coherent structures with length scale of $\Delta\theta \sim \pi/2$ can also be seen in the FFT.

4.3. *Mean velocity profiles*

In figure 13 we compare the mean streamwise velocity profiles with and without transpired walls and for different Reynolds numbers. It is observed that the mean streamwise velocity for non-transpired walls exhibits a dependence on the Reynolds number and differs significantly from the laminar profile. However, for transpired walls with strong injection, the mean streamwise velocity profiles are less dependent on the injection Reynolds number for each individual ϵ. In addition, although there

https://doi.org/10.1017/S0022112010005215 Published online by Cambridge University Press

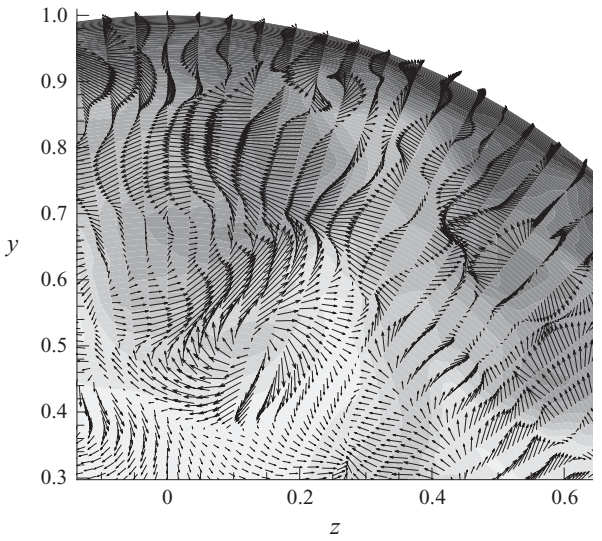


FIGURE 11. Enlarged view of the velocity field marked by a black box for the $\epsilon = 0.04$ case shown in figure 10(b). The arrows show the (u_r, u_θ) velocity vectors.

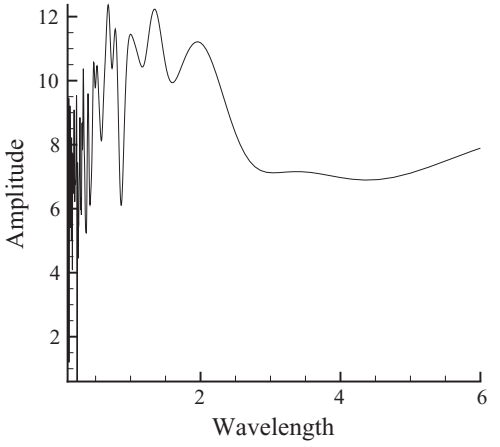


FIGURE 12. FFT as a function of wavelength in $\Delta\theta$ of the one-dimensional slice through $r = 0.5$ extracted from the flow field of the $\epsilon = 0.04$ case in figure 10.

are differences between the turbulent and the laminar profile (the Taylor–Proudman–Culick profile), the differences are small compared with the non-transpired wall case.

4.4. *Root mean square*

In figure 14 the u_x-r.m.s. velocity near the wall is plotted and shows a dependence on the injection Reynolds number. We point out that away from the wall, the u_x-r.m.s. velocity becomes less dependent on the Reynolds number. A comparison of the mean and r.m.s. streamwise velocity components is shown in figure 15 for both transpired and non-transpired wall cases. It can be seen that the magnitude of the r.m.s. is smaller than the mean for non-transpired walls, whereas there is a thin layer near the injection surface where the magnitude of the r.m.s. is larger than the mean for the transpired wall case. Therefore, the near-wall shear is dominated by the r.m.s.

https://doi.org/10.1017/S0022112010005215 Published online by Cambridge University Press

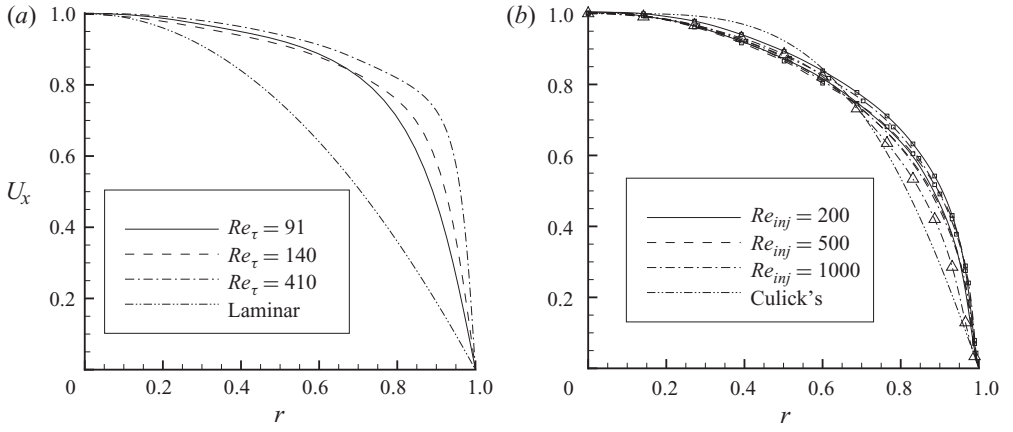


FIGURE 13. Plot of the mean streamwise velocity profiles, normalized by the mean centreline velocity, for flows with (*a*) no injection and (*b*) strong injection with $\epsilon = 0.1$ (△), 0.025 (□) and 0.04 (no symbol). Laminar solutions are shown as the dot-dot-dashed curves.

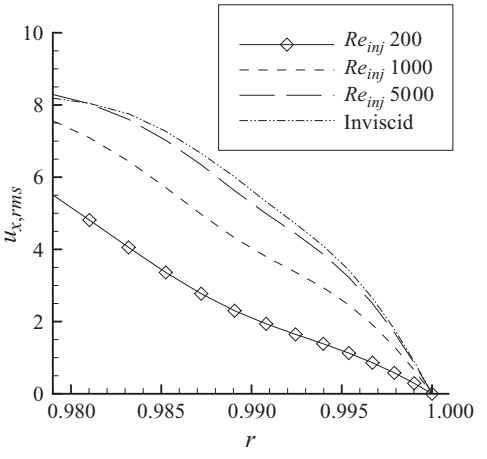


FIGURE 14. The near-wall u_x-r.m.s. velocity profiles with $\epsilon = 0.04$ and for different injection Reynolds numbers.

in the transpired wall case; for the non-transpired wall case, the near-wall shear is dominated by the mean. Also note that the mean streamwise velocity profile for the transpired wall case has an inflection point near the injecting surface, in agreement with the earlier findings of Nicoud *et al.* (1995). The presence of an inflection point could have important stability considerations.

4.5. *Statistics*

The nature of injection-driven turbulence in cylindrical geometry is expected to be qualitatively similar to that in planar geometry in terms of spatial trends and relative magnitudes of different terms in the mean and Reynolds stress equations. We therefore refer to Venugopal *et al.* (2008) for statistical equations and details of these characteristics. Here, we present only representative statistics.

Profiles of the r.m.s. velocities ($u_{x,rms}$, $u_{r,rms}$, $u_{\theta,rms}$) are shown in figure 16(*a*). Note that near the axis at $r = 0$, the r.m.s. of the radial and circumferential components

https://doi.org/10.1017/S0022112010005215 Published online by Cambridge University Press

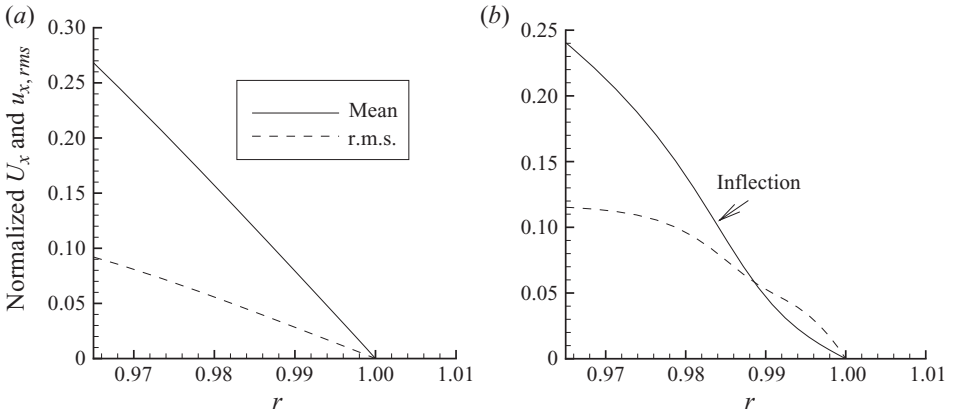


FIGURE 15. Plots of the mean and the r.m.s. of the streamwise velocity, normalized by the mean centreline velocity, for (*a*) non-transpired ($Re_\tau = 141$) and (*b*) transpired ($Re_{inj} = 1000$) flows. For the transpired wall case, the location of the inflection point of the mean streamwise velocity is denoted by an arrow.

are almost identical asymptotically, as may be expected because of the removable singularity there. Also note that the r.m.s. increases as ϵ decreases. Figure 16(*b*) shows the mean viscous stress term

$$\frac{1}{Re}\frac{1}{r}\frac{\partial}{\partial r}\left(r\frac{\partial \bar{u}_x}{\partial r}\right) \tag{4.1}$$

in the mean streamwise momentum equation for different injection Reynolds numbers with $\epsilon = 0.04$. Note that as the injection Reynolds number increases, both the thickness of the layer in which the viscous stress is important and the amplitude of the stress decreases. The production of turbulent kinetic energy

$$\overline{u_i' u_r'}\,\frac{\partial u_i}{\partial r} \tag{4.2}$$

in the mean kinetic energy equation is shown in figure 16(*c*) and has a profile similar to that in planar geometry (figure 16*a* of Venugopal *et al.* 2008). The viscous dissipation in the turbulent kinetic energy equation is plotted in figure 16(*d*). For simplicity we use the term

$$-\frac{1}{Re}\overline{\left[\left(\frac{\partial u_x'}{\partial r}\right)^2 + 2\left(\frac{\partial u_r'}{\partial r}\right)^2 + \left(\frac{\partial u_\theta'}{\partial r}\right)^2\right]} \tag{4.3}$$

to characterize the viscous dissipation in cylindrical geometry; the other terms can be neglected especially near the wall. Consistent with the planar results of Venugopal *et al.* (2008), the figure shows that the viscous dissipation attains its maximum away from the wall for the transpired case, which is fundamentally different from the non-transpired wall case in which the maximum occurs at the wall.

4.6. *Scaling for turbulent viscosity*

As discussed above, the near-wall shear is dominated by the r.m.s. in the transpired wall case, and a scaling velocity based on the shear at the wall should naturally account for this fact. Thus, for flows with transpired walls, we propose a wall-friction velocity

$$u_{\tau,inj} = \sqrt{\tau_{w,inj}/\rho} \tag{4.4}$$

https://doi.org/10.1017/S0022112010005215 Published online by Cambridge University Press

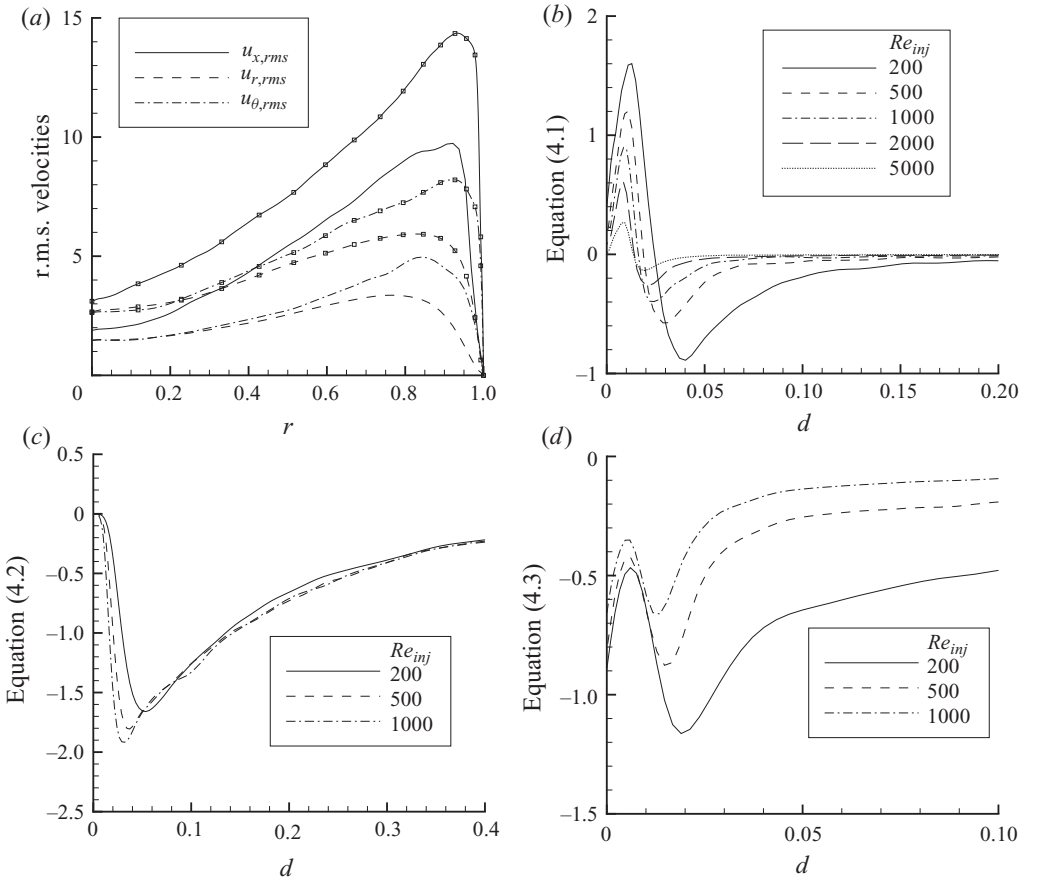


FIGURE 16. (*a*) Profiles of the r.m.s. velocities in a three-dimensional cylindrical multi-scale simulation with $Re_{inj} = 1000$ and for $\epsilon = 0.04$ (no symbols) and 0.025 (symbols). (*b–d*) Plots of the near-wall profiles of the following, for different injection Reynolds numbers and $\epsilon = 0.04$: (*b*) mean viscous stress term in the mean streamwise momentum equation normalized by $\bar{u}_b = 2\int_0^1 r\bar{u}\,\mathrm{d}r$, (*c*) production of turbulent kinetic energy term normalized by $\bar{u}_b^2$ and (*d*) the viscous dissipation in the turbulent kinetic energy equation normalized by the averaged production of turbulent kinetic energy.

for turbulent viscosity with τ_w based on the sum of the mean and the r.m.s. of the streamwise velocity, i.e.

$$\tau_{w,inj} = \mu \left| \frac{\partial(\bar{u}_x + u_{rms})}{\partial r} \right|_w . \tag{4.5}$$

Figure 17 plots the ratio of the turbulent eddy viscosity to the laminar kinematic viscosity, ν_t/ν_L, as a function of the distance from the injecting surface and for two different values of ϵ, the multi-scale parameter. Figure 17(*a*) plots the data as a function of $d = 1 - r$ (i.e. no scaling); figure 17(*b*) plots the data as a function of $d_c^+ = (1 - r)u_\tau/\nu$, which is the classical scaling; and figure 17(*c*) plots the data as a function of the new scaling $d^+ = (1 - r)u_{\tau,inj}/\nu$ proposed here. As can be seen in figure 17(*c*), profiles of ν_t/ν_L at different injection Reynolds numbers and different values of ϵ coalesce after the scaling. The data can be fitted by

$$\nu_t/\nu_L = 0.0011(d^+)^{3.5}, \tag{4.6}$$

https://doi.org/10.1017/S0022112010005215 Published online by Cambridge University Press

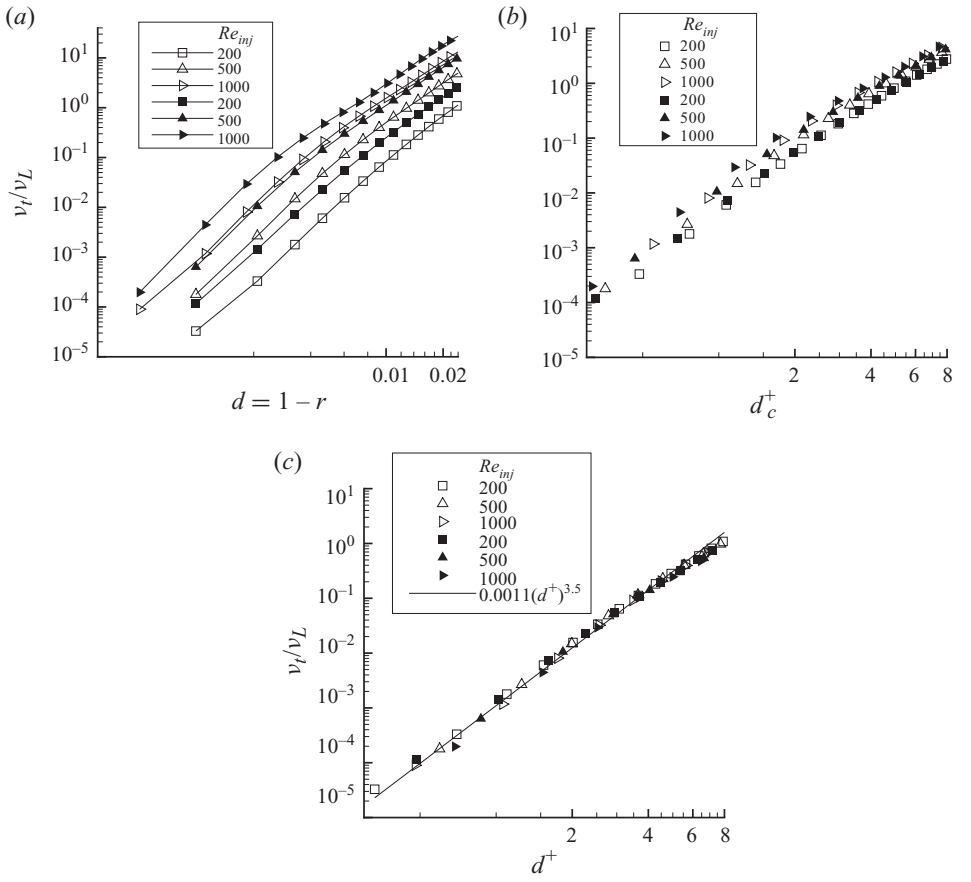


FIGURE 17. Plot of the ratio of the turbulent to the laminar viscosity of flows with transpired walls as a function of (*a*) $d = 1 - r$, (*b*) $d_c^+ = (1 - r)u_\tau/\nu$ and (*c*) $d^+ = (1 - r)u_{\tau,inj}/\nu$ and for ϵ values of 0.04 (open symbols) and 0.025 (filled symbols). Note that $u_{\tau,inj} = \sqrt{\tau_{w,inj}/\rho}$ with $\tau_{w,inj}$ given by (4.5).

which can serve as a turbulence subgrid model near the wall. By contrast, for the scaling with the classical wall-friction velocity shown in figure 17(*b*), based on τ_w and given by (3.16), the data do not coalesce as closely. Note that for cylindrical geometry, ν_t is obtained from (3.14).

We are not aware of any previous discussions or results on the power law fit of near-wall turbulent viscosity as a function of distance from the surface for flows with strong injection. The validation of the power of 3.5 has to be sought through experiments like those in DeGraaff & Eaton (2000), but for flows with strong injection, or like those in Deng, Adrian & Tomkins (2002).

4.7. *Estimates of near-wall shear*

As mentioned in the Introduction, (1.1) is used as a model for the shear near the propellant surface in our studies of erosive burning (Buckmaster & Jackson 2000; Isfahani *et al.* 2009; Zhang & Jackson 2010). To give support to the shear model, we examine the spatial and temporal behaviour of the shear at the injection surface. The instantaneous shear rate is estimated on the basis of the instantaneous streamwise

https://doi.org/10.1017/S0022112010005215 Published online by Cambridge University Press

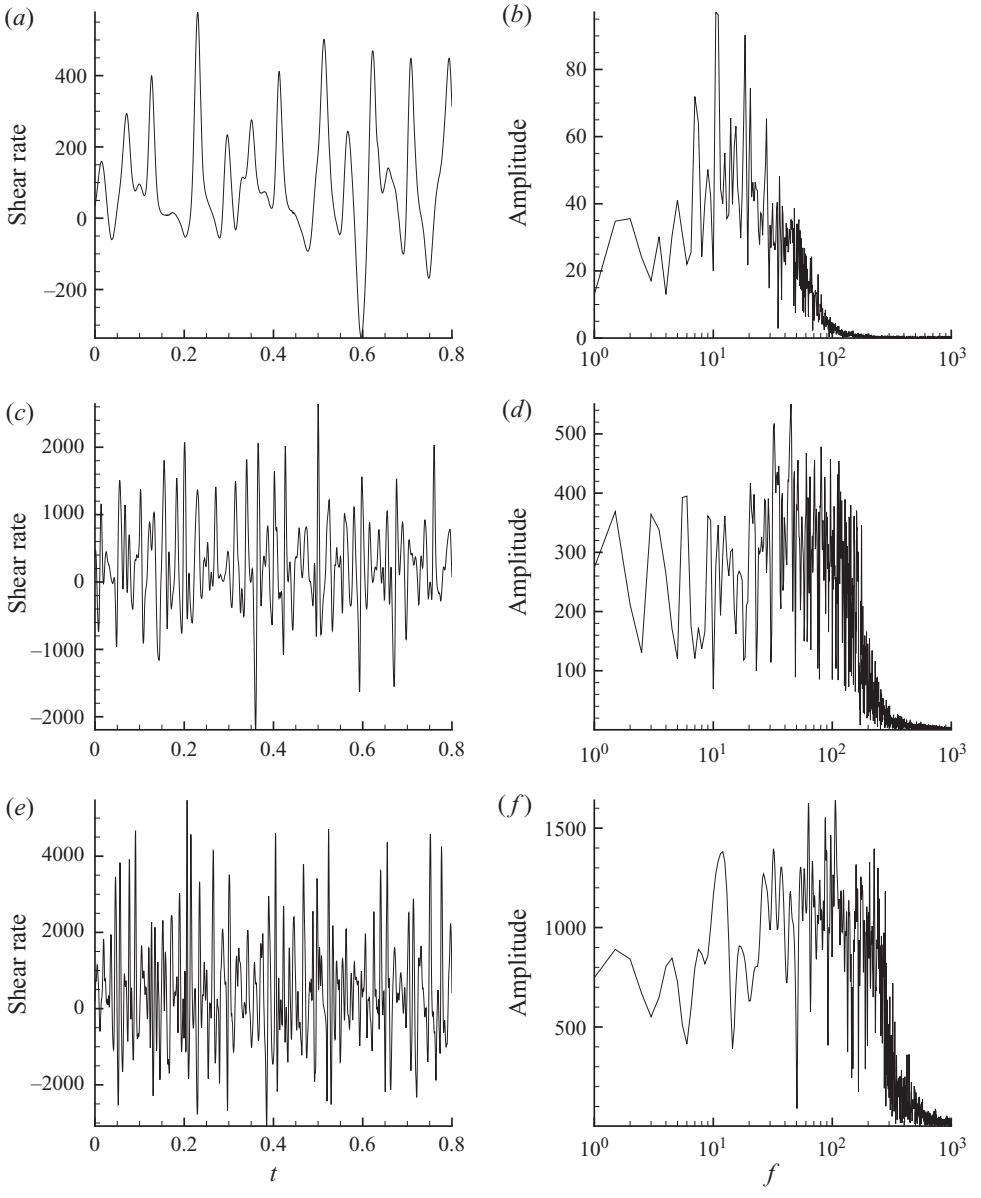


FIGURE 18. (*a*,*c*,*e*) Non-dimensional shear profiles as a function of non-dimensional time. (*b*,*d*,*f*) The corresponding FFTs. Here, $\epsilon = (a,b)\ 0.1$, $(c,d)\ 0.04$ and $(e,f)\ 0.025$, with $Re_{inj} = 1000$. The shear rate is obtained on the basis of the instantaneous streamwise velocity at the first grid point away from the surface, i.e. $|\partial u_x/\partial r| \approx u_x|_{r=1-\Delta r}/\Delta r$.

velocity at the first grid point away from the wall, i.e. $|\partial u_x/\partial r| \approx u_x|_{r=1-\Delta r}/\Delta r$, and is a function of both space and time.

Figure 18 shows the shear rates as a function of time at one spatial location and the corresponding FFTs, for $\epsilon = 0.1, 0.04, 0.025$ and $Re_{inj} = 1000$. The profiles show that near the head end ($\epsilon = 0.1$) the flow is less turbulent than farther downstream ($\epsilon = 0.025$). There is also a corresponding increase in the shear amplitude with decreasing ϵ. There is a shift in the dominant frequencies from low ($\sim$10) for $\epsilon = 0.1$

https://doi.org/10.1017/S0022112010005215 Published online by Cambridge University Press

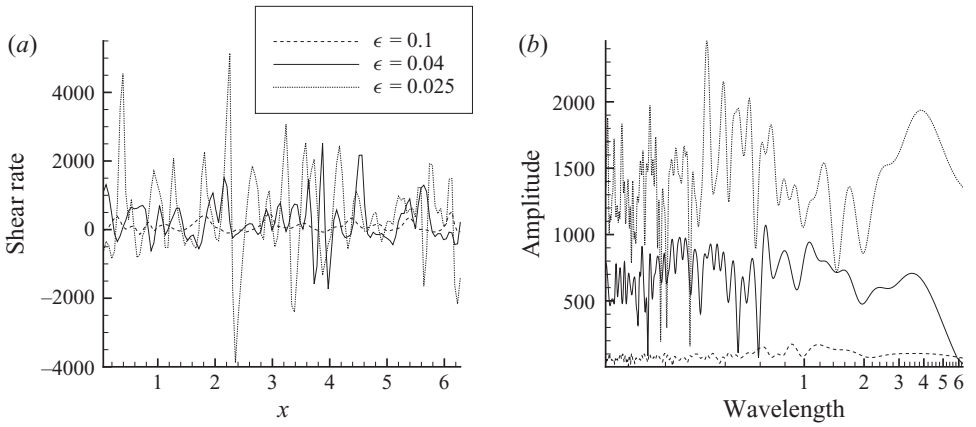


FIGURE 19. (*a*) Non-dimensional shear rates as a function of x. (*b*) The corresponding FFTs. Here, $\epsilon = 0.1$, 0.04 and 0.025. Note that the shear rates are periodic in x.

to high ($\sim$100) for $\epsilon = 0.025$. Both the shift in the dominant frequencies and the increase in the shear amplitudes are consistent with the trends observed in the VECLA experiments shown in figure 8 of Fabignon *et al.* (2003), partially validating our results here. Note that the experiments are planar, and therefore a direct comparison is not meaningful.

Figure 19 shows the shear rates as a function of space at one instant of time and the corresponding FFTs, for $\epsilon = 0.1, 0.04, 0.025$ and $Re_{inj} = 1000$. It is observed that for large values of ϵ (near the head end), long wavelengths $O(1)$ dominate because of the relatively organized flow structure. On the other hand, for small ϵ values (downstream), the strength of components with short wavelengths starts to increase or dominate because of the stronger developed turbulence. As discussed in § 4.1, the grid resolution of $n_x = 128$ for the streamwise direction is apparently inadequate for small ϵ values, as there are still significant powers at short wavelengths and high wavenumbers. Therefore, we are not quite in the position to answer the question of what is the range of dominant length scales near the wall, an important question for erosive burning of homogeneous propellants (Zhang & Jackson 2010). However, we have demonstrated for $\epsilon = 0.04$ in § 4.1 that once we increase the number of grid points in the streamwise direction, n_x, from 128 to 256, the resolution is appreciably improved; thus, we believe that it would be adequate once n_x reaches $\sim$1000. This implies that the dominant wavelength is $\sim[2\pi/500, 2\pi]$, within the range of wavelengths assumed in Zhang & Jackson (2010).

Another feature to note in figure 9 is that away from the wall, the flow becomes 'less turbulent' with weaker vorticity and structures with larger length scales than near the wall. This is confirmed by examining figure 20 for the streamwise u_x profiles along $r = 0.5$ and for various values of ϵ.

Figure 21 plots the shear rate as a function of space and time for two different values of ϵ. The corresponding FFTs for $\epsilon = 0.025$ are shown in figure 22. An examination of these figures does not reveal any localized regions of unusual dynamics, and therefore, using information at a particular spatial location or at a particular instant of time to estimate shear amplitudes, frequencies and wavelengths is justified.

From figure 21 one can observe the semi-characteristic nature of the shear rates in the space–time domain. These semi-characteristics closely resemble the characteristics of a wave equation due to the hyperbolic nature of the governing equations. We refer

https://doi.org/10.1017/S0022112010005215 Published online by Cambridge University Press

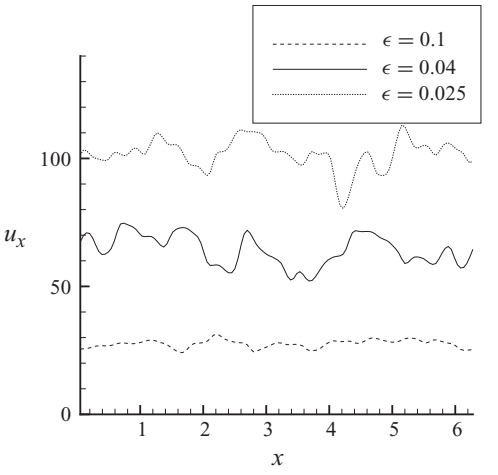


FIGURE 20. One-dimensional slices of u_x velocity at $r = 0.5$ for different ϵ values.

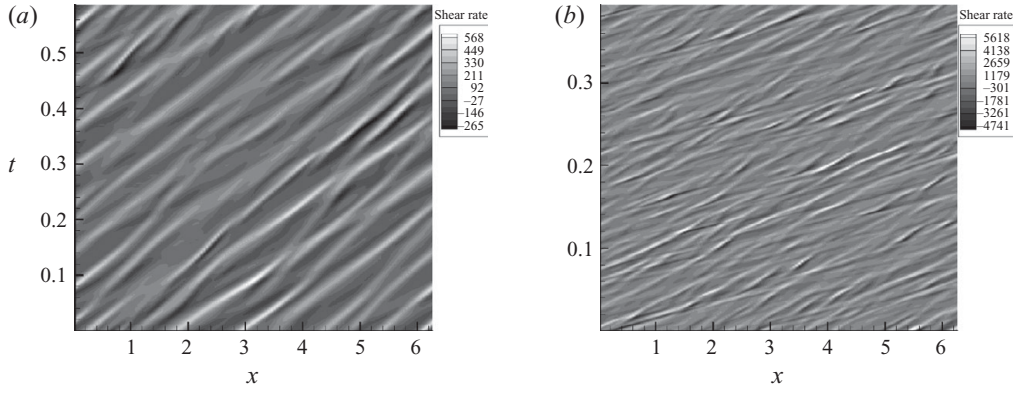


FIGURE 21. Shear rates as a function of both space and time for $\epsilon = (a)$ 0.1 and (b) 0.025.

to them as semi-characteristics for the obvious reason that they are not pure waves because of the presence of viscosity. These semi-characteristics are associated with the propagation of shear waves downstream. The wave speeds c can be derived from the slopes of the semi-characteristics. For $\epsilon = 0.025$ a non-dimensional wave speed of ~ 35 seems to be reasonable. This corresponds to the dominant frequency of ~ 80 in figure 18 and the wavelength of ~ 0.5 from figure 19(b); i.e. $c = \lambda f = 0.5 \times 80 = 40$. For $\epsilon = 0.1$ the wave structure is much simpler and better resolved, and the dominant wavelength and frequency are easier to identify. A wave speed of ~ 10 is observed and corresponds to that based on the dominant frequency of ~ 10 and wavelength of ~ 1 obtained from the data shown in figures 18 and 19, respectively.

4.8. *Erosive-burning modelling*

The erosive-burning models proposed by Buckmaster & Jackson (2000), Isfahani *et al.* (2009) and Zhang & Jackson (2010) require estimates for the shear amplitude, wavelength and frequency for (1.1). Typically, the shear cannot be measured experimentally; however, it is related to the mean crossflow velocity which can be measured. And therefore in figure 23(a) we plot the non-dimensional crossflow

https://doi.org/10.1017/S0022112010005215 Published online by Cambridge University Press

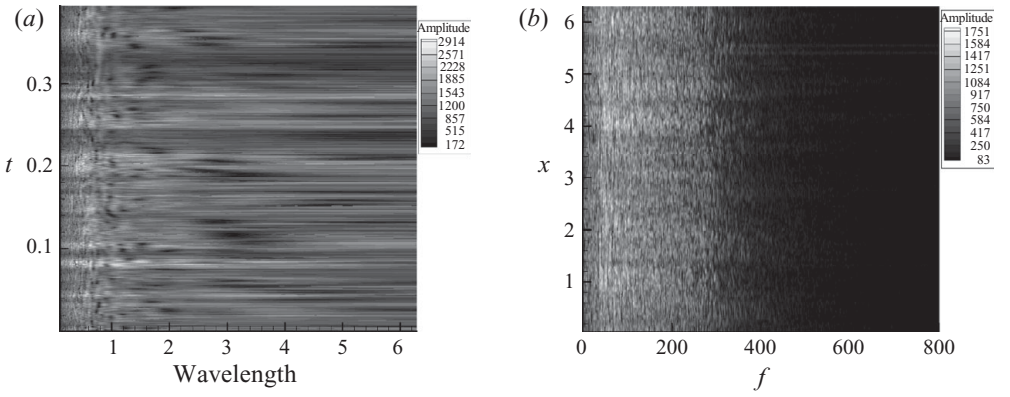


FIGURE 22. FFTs as a function of (a) the wavelength at different instants of time and (b) the frequency at different streamwise locations. Data are extracted from figure 21(b) for $\epsilon = 0.025$.

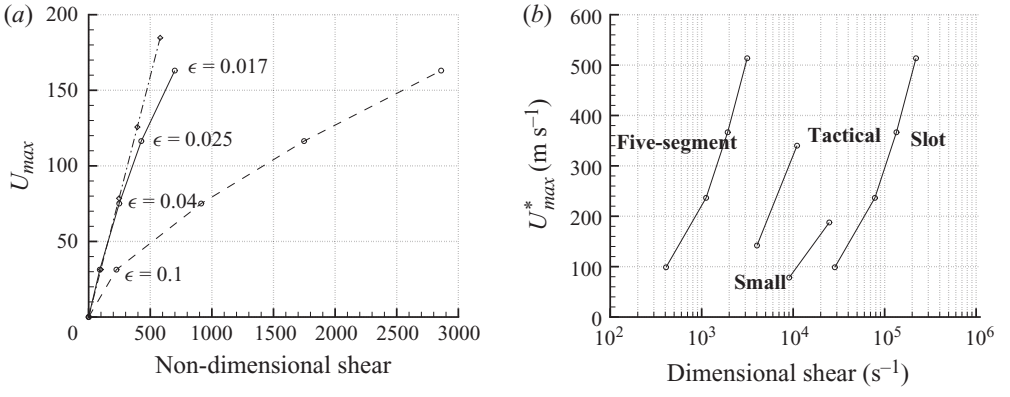


FIGURE 23. (a) Plot of the non-dimensional crossflow velocity as a function of the non-dimensional shear rate. See text for description of line styles. (b) Plot of the dimensional crossflow velocity as a function of the dimensional shear rate for a variety of motor geometries (see table 1). Here, $Re_{inj} = 1000$.

velocity as a function of the non-dimensional shear. The non-dimensional crossflow velocity is defined as the mean streamwise velocity at $r = 0$. The non-dimensional shear rate is defined as the streamwise velocity gradient at the injection surface in the wall-normal direction, i.e. $|\partial u_x/\partial r|$ evaluated at $r = 1$. The dot-dashed curve shown in the figure corresponds to Culick's solution, given by

$$U_x = \pi x \cos\left(\frac{\pi r^2}{2}\right), \tag{4.7}$$

so that the corresponding maximum streamwise velocity is $U_{max} = \pi x = \pi/\epsilon$, and the corresponding shear rate at the surface is given by $|\partial U/\partial r| = \pi^2 x = \pi^2/\epsilon$. The solid (mean only) and dashed (mean + r.m.s.) curves are solutions obtained from the multi-scale simulations. Note that there is little difference between Culick's solution (the dot-dashed curve) and the solid curve for the means. However, the magnitude of the velocity fluctuations near the surface is large, giving rise to large r.m.s. values. Thus, the shear rate based on the mean and the r.m.s. is significantly larger than the shear rate based on the mean only.

https://doi.org/10.1017/S0022112010005215 Published online by Cambridge University Press

Parameter	Small	Tactical	Space shuttle	Slot
Radius, h (m)	0.025	0.102	0.700	0.01
Length, L (m)	0.6	2.03	41.0	1.0
v_{inj} (m s^{-1})	2.5024	4.5322	3.1487	3.1487
Frequency, f (Hz)	$[1 \times 10^3, 5 \times 10^3]$	[453, 2265]	[45, 360]	$[3149, 3.15 \times 10^4]$
Re_{inj}	[700, 3000]	$[3000, 1 \times 10^4]$	$[1 \times 10^4, 1 \times 10^5]$	[300, 1000]

TABLE 1. Parameters and ranges of the injection Reynolds number $Re_{inj} = v_{inj}h/\nu$ for several representative motors.

The dashed curve in figure 23(a) is a universal curve and must be properly interpreted for a particular geometry. We therefore shed light on the dimensional values of the amplitude of the shear based on the non-dimensional results. Using the non-dimensional mean-plus-r.m.s. curve of figure 23(a), we plot in figure 23(b) the dimensional crossflow velocity as a function of dimensional shear for various motor geometries, the parameters of which are listed in table 1. Relevant ranges of the injection Reynolds number for motors of different sizes are also given in the table for typical operating conditions with a temperature range of 2400–3000 K and a pressure range of 10–100 atm. To determine the axial location corresponding to the crossflow velocity and shear rate, use $X = h/\epsilon$. For example, for the small motor, there are only two points plotted which correspond to $\epsilon = 0.1$ and 0.04, giving the axial locations of $X =$ 0.25 and 0.625 m, respectively, with the last value roughly corresponding to the aft end of the motor.

In the calculations for figure 23(b), lengths are scaled by the chamber radius h (in m), velocities by the injection velocity v_{inj} (in m s^{-1}) and time by h/v_{inj} (in s). The dimensional frequency ranges from the head to the aft end are given in table 1 with typical non-dimensional frequencies of $\sim$10, 50, 80 and 100 for ϵ values of 0.1, 0.04, 0.025 and 0.017, respectively, based on the results from the previous subsection. In each curve the value corresponding to the smallest crossflow velocity corresponds to an axial location near the head end, while the largest crossflow velocity corresponds to an axial location near the aft end. In this manner a relationship between the magnitude of the shear and the crossflow velocity can be obtained.

5. Concluding remarks

We have performed DNS of an incompressible turbulent flow in a periodic circular pipe with transpired walls, as a model for the core flows in SRMs. The injection is assumed to be strong, and hence there is no boundary layer at the injection surface. The model is based on a multi-scale asymptotic approach.

We first validated our flow solver with simulations of turbulent channel/pipe flows with non-transpired or transpired walls with weak injection. The results were shown to agree with the theory and the numerical results by others, strengthening our confidence in the results of turbulent flows with transpired walls with strong injection. However, validation for the complete multi-scale equations given by (2.7) is not possible at the present time because of the lack of appropriate experimental data for cylindrical geometry.

Unlike flows with non-transpired walls, the mean streamwise velocity depends only weakly on the injection Reynolds number. However, the r.m.s. of the streamwise velocity does show a dependence on the Reynolds number. The mean streamwise

https://doi.org/10.1017/S0022112010005215 Published online by Cambridge University Press

velocity profile has an inflection point near the injecting surface, in agreement with the earlier findings of Nicoud *et al.* (1995). The presence of an inflection point could have important stability considerations. Also, there is a thin layer in which the magnitude of the r.m.s. is larger than the mean streamwise velocity for the transpired wall case, whereas the magnitude of r.m.s. is always smaller than the mean in flows with non-transpired walls. As a result, a new wall-friction velocity based on the total shear derived from the sum of both the mean and r.m.s. streamwise velocities is introduced for turbulent flows with transpired walls, and it is shown to produce encouraging scaling for turbulent viscosity. A $d^{3.5}$ dependence for turbulent viscosity is also found with d being the distance from the injecting surface.

This work was supported by the US Department of Energy through the University of California under subcontract B523819 and by the NASA Constellation University Institutes Project under grant NCC3-989 through the University of Maryland with a subcontract Z634015 to the University of Illinois at Urbana-Champaign, with Claudia Meyer as the project manager.

REFERENCES

Apte, S. V. & Yang, V. 2003 A large-eddy simulation study of transition and flow instability in a porous-walled chamber with mass injection. *J. Fluid Mech.* **477**, 215–225.

Avalon, G., Ugurtas, B., Grisch, F. & Bresson, A. 2000 Numerical computations and visualization tests of the flow inside a cold gas simulation with characterization of a parietal vortex shedding. *AIAA Paper* 2000-3387.

Buckmaster, J. & Jackson, T. L. 2000 The effects of time-periodic shear on a diffusion flame anchored to a propellant. *Combust. Flame* **120**, 211–221.

Cabrit, O. & Nicoud, F. 2009 Direct simulations for wall modeling of multicomponent reacting compressible turbulent flows. *Phys. Fluids* **21**, 055108.

Culick, F. E. C. 1966 Rotational axisymmetric mean flow and damping of acoustic waves in solid propellant rocket motors. *AIAA J.* **4**, 1462–1464.

DeGraaff, D. B. & Eaton, J. K. 2000 Reynolds number scaling of the flat-plate turbulent boundary layer. *J. Fluid Mech.* **422**, 319–346.

Deng, Z., Adrian, R. J. & Tomkins, C. D. 2002 Sensitivity of turbulence in transpired channel to injection velocity small-scale non-uniformity. *AIAA J.* **11**, 2241–2246.

Eggels, J. G. M., Westerweel, J., Nieuwstadt, E. T. M. & Adrian, R. J. 1993 Direct numerical simulation of turbulent pipe flow. *Appl. Sci. Res.* **51**, 319–324.

Fabignon, Y., Dupays, J., Avalon, G., Vuillot, F., Lupoglazoff, N., Casalis, G. & Prevost, M. 2003 Instabilities and pressure oscillations in solid rocket motors. *Aerosp. Sci. Technol.* **7**, 191–200.

Green, L. 1954 Erosive burning of some composite solid propellants. *Jet Propul.* **24**, 9–15.

Hu, F. Q., Hussaini, M. Y. & Manthey, J. L. 1996 Low-dissipation and -dispersion Runge–Kutta schemes for computational acoustics. *J. Comput. Phys.* **124**, 177–191.

Isfahani, A. H. G., Zhang, J. & Jackson, T. L. 2009 The effects of turbulence-induced time-periodic shear on a flame anchored to a propellant. *Combust. Flame* **156**, 1084–1098.

Jiang, G. S. & Shu, C.-W. 1996 Efficient implementation of weighted ENO schemes. *J. Comput. Phys.* **126**, 202.

Kim, J. & Moin, P. 1985 Application of a fractional-step method to incompressible Navier–Stokes equations. *J. Comput. Phys.* **59**, 308–323.

Kim, J., Moin, P. & Moser, R. 1987 Turbulence statistics in fully developed channel flow at low Reynolds number. *J. Fluid Mech.* **177**, 133–166.

King, M. K. 1993 Erosive burning of solid propellants. *J. Propul. Power* **9**, 785–805.

Lupoglazoff, N. & Vuillot, F. 1996 Parietal vortex shedding as a cause of instability for long solid propellant motors – numerical simulations and comparisons with firing tests. *AIAA Paper* 96-0761.

https://doi.org/10.1017/S0022112010005215 Published online by Cambridge University Press

Lupoglazoff, N. & Vuillot, F. 1998 Numerical simulations of parietal vortex-shedding phenomenon in a cold flow set-up. *AIAA Paper* 98-3220.

Moser, R. D., Kim, J. & Mansour, N. N. 1999 Direct numerical simulation of turbulent channel flow up to $Re_\tau = 590$. *Phys. Fluids* **11** (4), 943–945.

Nicoud, F. C. & Angilella, J. R. 1997 Effects of uniform injection at the wall on the stability of Couette-like flows. *Phys. Rev.* E **56**, 3, 3000–3009.

Nicoud, F. C., Poinsot, T. J. & Ha Minh, H. 1995 Direct numerical simulation of turbulent flow with massive uniform injection. In *10th Symposium on Turbulent Shear Flows, Pennsylvania State University, University Park, PA*.

Proudman, I. 1960 An example of steady laminar flow at large Reynolds number. *J. Fluid Mech.* **9**, 593–602.

Spalart, P. 1988 Direct simulation of a turbulent boundary layer up to $Re_\theta = 1410$. *J. Fluid Mech.* **187**, 61–98.

Spalding, D. B. 1961 A single formula for the law of the wall. *J. Appl. Mech.* **28**, 455–457.

Stevenson, T. N. 1963 A law of the wall for turbulent boundary layers with suction or injection. *Aero Rep.* 166. Cranfield College of Aeronautics.

Sumitani, Y. & Kasagi, N. 1995 Direct numerical simulation of turbulent transport with uniform wall injection and suction. *AIAA J.* **33**, 1220–1228.

Taylor, G. I. 1956 Fluid flow in regions bounded by porous surfaces. *Proc. R. Soc. Lond.* A **234**, 456–475.

Traineau, J. C., Hervat, P. & Kuentzmann, P. 1986 Cold flow simulation of a two dimensional nozzleless solid rocket motor. *AIAA Paper* 86-1447.

Venugopal, P., Moser, R. D. & Najjar, F. M. 2008 Direct numerical simulation of turbulence in injection driven plane channel flows. *Phys. Fluids* **20**, 105103.

Wasistho, B. & Moser, R. D. 2005 Simulation strategy of turbulent flow in solid rocket motor. *J. Propul. Power* **21**, 251–263.

Zhang, J. & Jackson, T. L. 2009 A high-order incompressible flow solver with WENO. *J. Comput. Phys.* **228**, 2426–2442.

Zhang, J. & Jackson, T. L. 2010 A model for erosive burning of homogeneous propellants. *Combust. Flame* **157** (2), 397–407.

https://doi.org/10.1017/S0022112010005215 Published online by Cambridge University Press